One-step slot-die coating deposition of wide-bandgap perovskite absorber for highly efficient solar cells

Sophie Bernard, Sébastien Jutteau, Salim Mejaouri, Stefania Cacovich, Iwan Zimmermann, Armelle Yaiche, Stéphanie Gbegnon, Dominique Loisnard, Stéphane Collin, Aurélien Duchatelet, et al.

One-step slot-die coating deposition of wide-bandgap perovskite absorber for highly efficient solar cells

Sophie Bernard, Sébastien Jutteau, Salim Mejaouri, Stefania Cacovich, Iwan Zimmerman, Armelle Yaiche, Stéphanie Gbegnon, Dominique Loisnard, Stéphane Collin, Aurélien Duchatelet, Frédéric Sauvage, Jean Rousset.*

Sophie Bernard, Salim Mejaouri, Dr. Iwan Zimmermann, Stéphanie Gbegnon
Institut Photovoltaïque d'Île-de-France (IPVF). 18 Boulevard Thomas Gobert, 91120 Palaiseau, France.
E-mail: sophie-s.bernard@edf.fr

Dr. Sébastien Jutteau, Dr. Jean Rousset, Aurélien Duchatelet, Armelle Yaiche, Dominique Loisnard
EDF R&D, 7 Boulevard Gaspard Monge, 91120 Palaiseau, France
Institut Photovoltaïque d'Île-de-France (IPVF). 18 Boulevard Thomas Gobert, 91120 Palaiseau, France.

Dr. Frédéric Sauvage
LRCS, Laboratoire de réactivité et Chimie du Solide (CNRS UMR 7314), Université de Picardie Jules Verne, Hub de l'énergie, 15 Rue Baudelocque, 80039 Amiens, France

Dr Stefania Cacovich
CNRS, École Polytechnique, IPVF, UMR 9006, 18, Boulevard Thomas Gobert, 91120 Palaiseau, France

Dr. Stéphane Collin
Centre de Nanosciences et de Nanotechnologies (C2N), CNRS, Université Paris-Saclay, 10 boulevard Thomas Gobert, 91120 Palaiseau, France
Institut Photovoltaïque d'Ile-de-France, 18 boulevard Thomas Gobert, 01120 Palaiseau, France

Keywords: perovskite solar cells, slot-die-coating, one-step deposition, upscale, STEM, stability

Abstract: Slot-die coating is a promising technique paving the way for large-area perovskite deposition and commercially relevant solar devices fabrication with sharp control over the thickness and material composition. However, before transferring perovskite solar cells technology to commercial applications, it is required to develop ink formulations guaranteeing

high homogeneity over wide surface and leading to large, defects-free and well-crystallized perovskite grains to maximize the device performances. We report a one-step slot-die deposition route, combining ink tailoring and vacuum aspiration solvent extraction affording the deposition of high bandgap multi-cation perovskite. One important key is the introduction of methylammonium chloride in the ink formulation which substantially enhances the film quality over large area. Although the efficacy of anti-solvent dripping is demonstrated on small area, it is not compatible with larger area. This work compares the latter with a vacuum quench protocol allowing efficient extraction of the solvents. Considering both ink formulation engineering and vacuum solvent extraction, we reached a stabilized power conversion efficiency of up to 17.5 %. This constitutes, to the best of our knowledge, the highest reported value for a high bandgap absorber deposited by slot-die coating. Moreover, stability over 180 hours under maximum power point conditions is herein demonstrated.

1. Introduction

Over the past ten years, the field of perovskite solar cells (PSCs) has known a tremendous development, rapidly increasing their power conversion efficiencies (PCE) from 3.8% [1] to 25.6% [2]. However, one of the key challenges to overcome before transferring this technology to commercial applications is the deposition of high quality and homogenous halide perovskite thin films on large areas. Today, the best performing PSCs are fully prepared by the spin-coating technique. Nonetheless, the latter affords homogenous coatings only on small area devices (ie. < 10 cm²). In addition, a large amount of precursor solution and solvent is wasted during spin-coating deposition, impeding its compatibility with cost-efficient large volume production [3]. Recently, new impetus is given to large area coating techniques, including blade-coating [4–8], inkjet [9,10] spray-coating [11,12] and slot-die coating [13–20]. It has been demonstrated that the slot-die coating method offers several advantages such as full compatibility with high

throughput production techniques line like roll-to-roll manufacturing, while allowing a sharp control over the uniformity on large areas [21]. Two deposition approaches have been developed for slot-die coating, ie. one-step deposition routes [13,15–17] in which all precursors are mixed into the same solution or two-step deposition routes where the PbI_2 and the organic layers are coated successively [18,19,22]. The formation of homogeneous and well-covering perovskite films requires both a fast trigger of the nucleation and delayed crystal growth. According to the LaMer model, which accounts well for the grain formation in lead halide perovskite [23], the nucleation onset is mainly controlled by the evacuation rate of the solvent after the deposition of the precursors. This is the role of the anti-solvent dripping to ensure a fast triggering of nuclei formation. However, this technique is not suitable for deposition on large areas and contributes to the generation of excessive chemical wastes in the elaboration process. To bypass this issue, in this work we elaborated a strategy combining ink formulation engineering and vacuum aspiration quench using a one-step slot-die coating method to reproduce the feat of the anti-solvent dripping while being fully compatible with large area deposition. The approach of vacuum solvent extraction has already been explored by several groups, mainly in association with spin-coated films [24,25]. Ding et al. demonstrated that a vacuum flash-assisted protocol (VASP) can convert the perovskite film within a few seconds [25]. Nonetheless, if a quasi-instantaneous drying is not achieved, a step necessary to swiftly reach the super-saturation threshold, the slowing-down of the crystal growth becomes a critical step to form a compact layer. In addition, recent studies have shown that the crystallization dynamic can be controlled by an accurate precursor ink formulation[26].

In this work, we focused on a double cation ($FA_{0.83}Cs_{0.17}$)/double anion $(I_{0.83}Br_{0.17})_3$ perovskite composition better suited to tandem applications owing to its high bandgap value (E_g = 1.64 eV) compared to $MAPbI_3$ counterpart. Engineering of the ink formulation by the introduction of methylammonium chloride (MACl) is herein studied, this additive being known to influence

the crystal growth [27–29]. Based on a holistic optimization of the triptych constituted by the ink formulation, the slot-die deposition parameters and the vacuum drying process, we achieved pinhole-free deposition on large area (5x10cm²) of $Cs_{0.17}FA_{0.83}Pb(I_{0.83}Br_{0.17})_3$ perovskite films. After their implementation into photovoltaic device, these layers allow to reach over 17.5% PCE stabilized (aperture area 0.09cm²), which is the best performance obtained so far for a high band gap absorber deposited by slot- die coating. Moreover, we demonstrated 90 % PCE retention on encapsulated devices after 180 hours under constant illumination and we characterized the degradation of the full devices by STEM technique (Scanning Transmission Electron Microscopy).

2. Results and discussion

2.1. Crystallization differences between vacuum extraction and anti-solvent method

First, the impact of the solvent evacuation method on the perovskite thin film formation has been studied. Perovskite layers have been fabricated by spin-coating, with a solvent extraction carried out either by anti-solvent (chlorobenzene dripping) or vacuum aspiration (5 minutes / 0.7 mbar). In contrast with the anti-solvent method which can evacuate the solvent almost instantaneously, the vacuum aspiration was expected to lead to a slower extraction rate. **Figure 1.a.** shows the top view by scanning electron microscopy (SEM) of perovskite films obtained with the two different quench processes. If no MaCl is added in the precursor solution, we notice that the anti-solvent dripping generates a denser and smoother morphology, compared to the one obtained with the vacuum quench, which exhibits multiple pinholes. Then, we compared the morphology of perovskite films obtained with three different (MACl: FAI) ratios, ranging 0 to 0.3. For the anti-solvent method, the grain size increases with the MACl content, which is coherent with the literature [30,31]. In the case of a vacuum quench, as the MACl concentration increases, the perovskite film becomes denser showing an enhanced coverage of

the substrate surface. K. Kosmatos et al. [32] suggested that, for a MAPI composition, MAI and PbI_2 coordinate to form colloidal frameworks in solution, underlining that the size and structure of these frameworks determine the morphology of the final perovskite film. In presence of MACl, these frameworks become larger and more stable due to the higher coordination of MACl with PbI_2 than MAI, leading to denser morphologies and wider grains and thus, enhanced devices performances. Moreover, this phenomenon has also been observed on FA-based perovskite composition, implying the relevance of this mechanism in the case of a PbI_2-FAI framework [33].

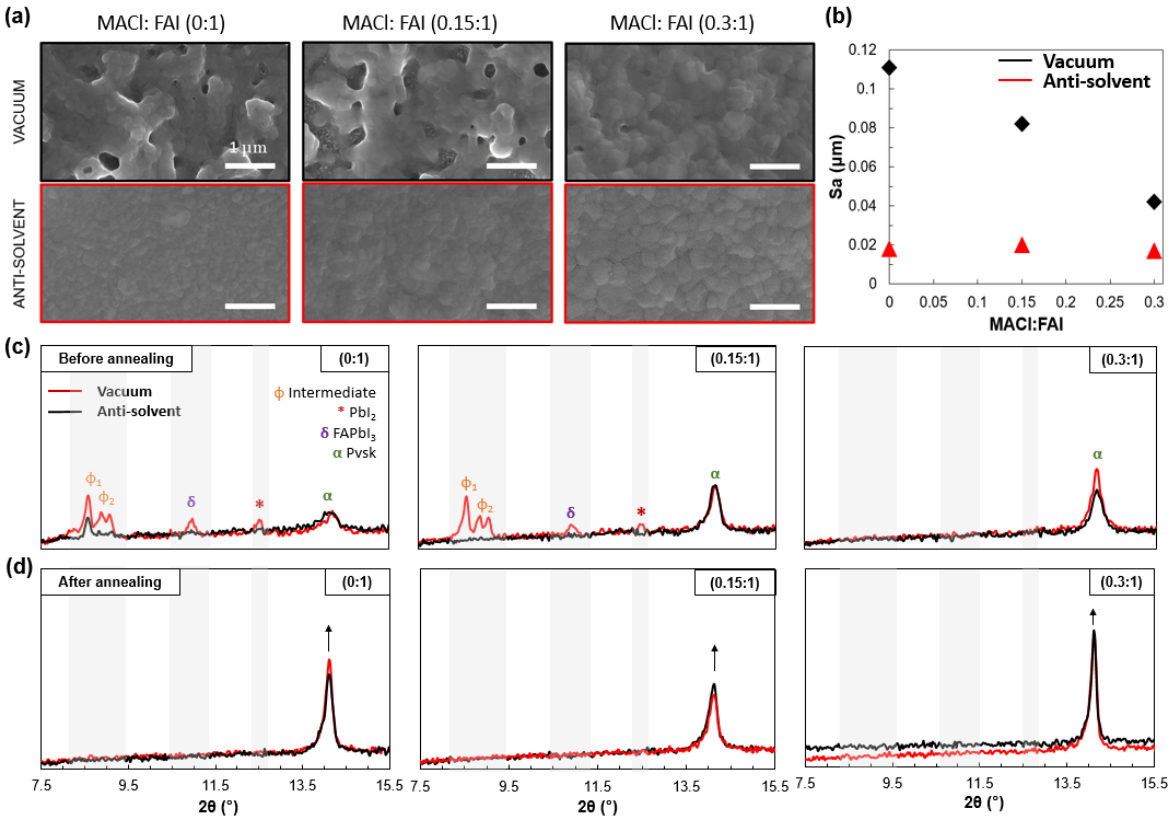

Figure 1 : Characterization of spin-coated films quenched either by anti-solvent or in a vacuum chamber with different MACl concentrations after annealing at 110°C during 30 min. a. Scanning Electron Microscopy (SEM) images of spin-coated perovskite layers. b. Sa measurements by confocal microscopy. c. XRD diffractograms of spin-coated layers before annealing and just after solvent extraction. The red curves represent perovskite layers quenched by anti-solvent dripping and the black curves stand for the vacuum quench. d. XRD diffractograms of spin-coated final perovskite layers after annealing.

From the confocal microscopy images (**Figure S 1),** we extracted the surface roughness Sa, which stands for the arithmetical mean roughness of the surface (**Figure 1.b.).** The MACl concentration increase lowers the surface roughness in case of a vacuum treatment (Sa value dropped from 111 nm to 42 nm). Contrariwise, the Sa value for the anti-solvent method remains stable (Sa ≈ 22 nm). Finally, the ratio MACl: FAI (0.3:1) leads to a comparable morphology between the two quench methods. The crystal properties were further studied by X-ray diffraction (XRD). Both perovskite layers, as deposited and annealed films have been characterized. In the case of the intermediate films (i.e. without post-treatment), the XRD measurements have been performed less than 3 min after the end of the quench **(Figure 1.c.)**. Despite the absence of a post-annealing and a swift transfer in the X-ray chamber, the perovskite photoactive α-phase is already present for all the conditions herein investigated, as shown by the presence of the diffraction peak at $2\theta = 14.1°$ corresponding to the (100) plans. In absence of MACl and regardless of the quenching method**,** we notice the presence of additional diffraction peaks which cannot be ascribed to the perovskite structure, a first peak at $2\theta = 8.6°$ attributed to a ϕ_1 phase, and two peaks at $2\theta = 8.9°$ and 9.1° attributed to a ϕ_2 phase. These two ϕ-phases are related to the formation of PbI_2 complexes involving the solvent molecules, PbI_2-DMF and PbI_2-NMP [34–36]. Interestingly, these diffraction peaks are gradually disappearing with the addition of MACl into the precursor solution. Such a phenomenon has already been noticed by Li et al. [37], who identified an identical trend, for double-cation MA/FA deposition by spin-coating. As suggested by Mateen et al. [27], MACl can efficiently coordinate with PbI_2, creating a new intermediate MACl-PbI_2-NMP/DMF. As a result, the introduction of an additional intermediate step allows for a better control of the growth rate before the solution reaches the supersaturation state [33]. At MACl: FAI (0.30:1), the solvent complexes signature,

PbI_2-DMF and PbI_2-NMP, is no longer present for both solvent extraction methods. Finally, when annealed, all the films demonstrate pure perovskite photoactive α-phase **(Figure 1.d.).**

2.2. Influence of MACl concentration on slot-die coated perovskite films

Based on the previous results, the influence of the MACl addition on the film formation using the slot-die coating method was investigated. The deposited films were quenched by the vacuum process using the same extraction time and pressure than for the spin-coated ones, and annealed at 110°C for 30 minutes. As previously highlighted, MACl addition decreases substantially the Sa value from 124 nm to 46 nm (**Figure 2.a and b**). **Figure 2.c and 2.d** compare the top view image of the slot-die coated perovskite film without MACl and with a 0.3:1 ratio of MACl. The film morphology is comparable to the perovskite layers obtained by spin-coating (see **Figure 1**). Thus, the beneficial effect of MACl is again demonstrated, leading to the formation of uniform and pinholes-free layers. Our results stress the advantageous effect of this additive and the versatility of this approach proving its transferability to scalable printing techniques.

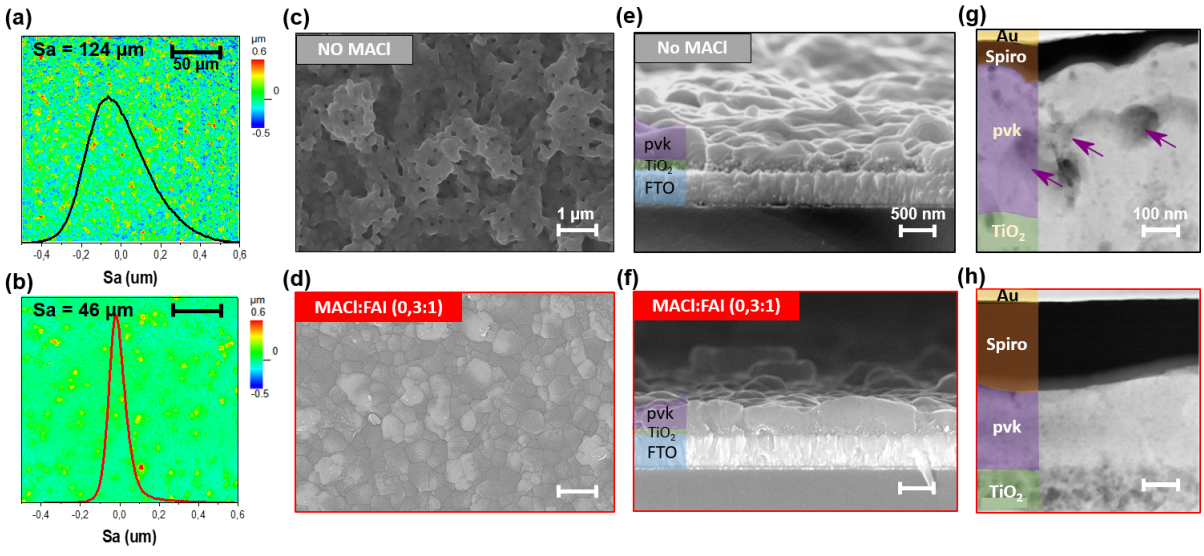

Figure 2 : Morphological characterization of post-annealed perovskite films fabricated by slot-die coating using vacuum quenching without and with MACl addition (Glass-FTO/c-TiO_2/m-TiO_2) (a. and b.) Roughness measurements deduced by confocal microscopy, **(c. and d.)** Top-view SEM images, **(e. and f.)** Cross-section SEM images. and **(g. and h.)** STEM-

HAADF images of complete device stack showing the different interfaces formed. The purples arrows are indicating pinholes formed within the perovskite layer

The improvement of the film compactness along the thickness is also observed on the cross-section SEM images (**Figure 2.e and f.**) with a clear decrease of the porosity and number of grain boundaries. To investigate further the morphology of the film implemented in full device solar cells, we used Scanning Transmission Electron Microscopy (STEM) to perform High Annular Angle Dark Field (HAADF) imaging. Each PSC constitutive layers are visible on the images presented in **Figure 2.g and 2.h**. The reference device (no MACl) exhibits porosity indicated with purple arrows and, in accordance with the previous observations, the perovskite film roughness decreases with the addition of MACl. The resulting X-ray diffractograms show exactly the same pattern than those obtained with the spin-coated films and the refined lattice cell parameter leads to a a value of 6.266(8) Å and 6.276(9) Å without and with 0.3 molar ratio of MACl, respectively **(Figure 3.a)**. These two similar values suggest that nor MA^+ neither Cl^- are introduced into the perovskite lattice[38] during the growth. Moreover, all the diffraction peaks can be indexed by the cubic Pm-3m space group, confirming the absence of impurities such as PbI_2 or non-photoactive δ-phase in the layer. The average crystallite size has been calculated using Williamson-Hall formalism assuming isotropic particles. The average crystallite size increases from 90 ± 8 nm to 152 ± 12 nm upon MACl addition in agreement with literature[28]. These results underline an enhancement of crystallinity as a result from crystal growth support. A more pronounced preferential orientation along the (100) direction compared to the (110) one is also observed suggesting that the MACl not only favours the crystal growth but also influences its orientation.

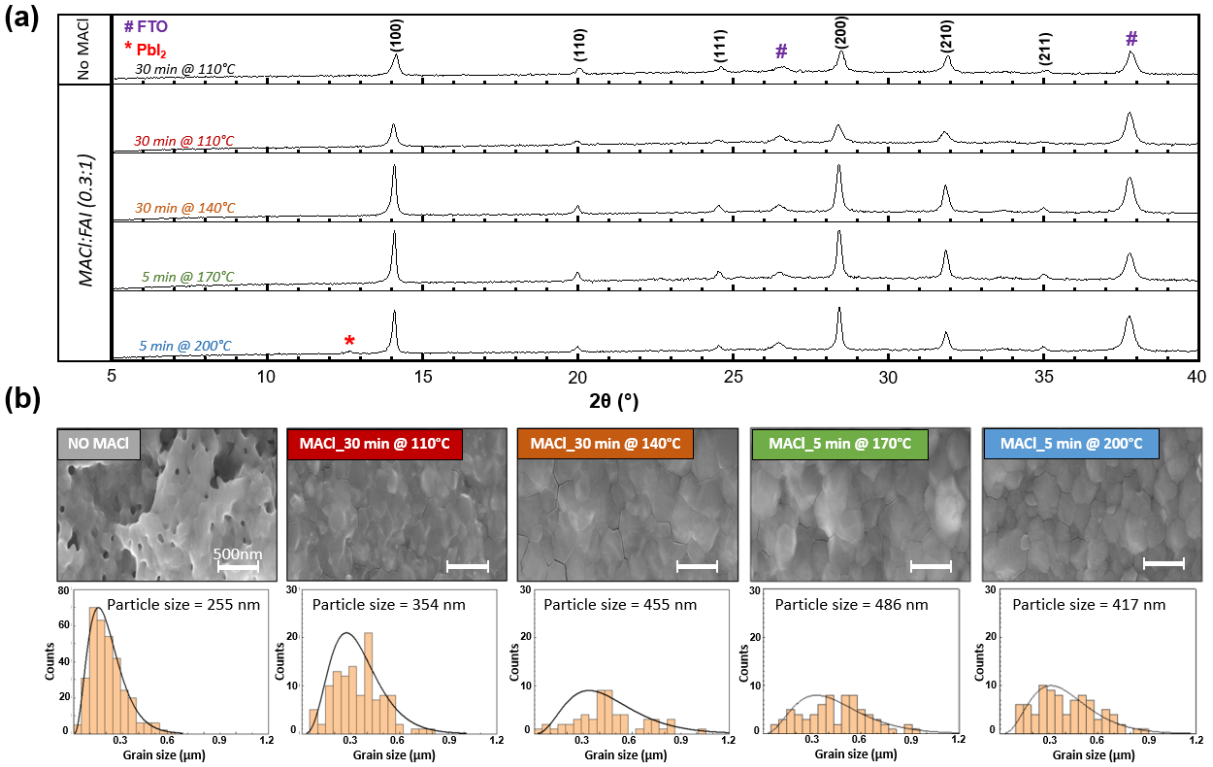

Figure 3: (a) X-ray diffractograms of the perovskite layers deposited on FTO/c-TiO_2/m-TiO_2 with and without MACl under different annealing conditions, **(b)** Top-view SEM images and associated grain size distribution.

The influence of the post-annealing conditions on the perovskite crystallization keeping the MACl: FAI ratio set at 0.3:1 was examined. Two "standard" post-treatment, at 110°C and 140°C for 30 minutes, and two "flash" ones, at 170°C and 200°C for 5 minutes were investigated. Except for the annealing at 200°C, which exhibits a small diffraction peak at 2θ = 12.6° corresponding to PbI_2 impurities that originate from the thermal degradation of the perovskite layer, all the other conditions are leading to pure α-phase (**Figure 3.a**). In any case, no noticeable shift of the X-ray diffraction peaks indicating a lattice cell parameter modification is observed. This indicates that neither change of stoichiometry nor MACl inclusion is expected when varying the annealing conditions. This latter, should have led to a lattice shrinkage due to the smaller size of the MA-cation compared to the FA-cation as pointed out by Nie et al.Erreur ! Source du renvoi introuvable.[39]. Moreover, the crystallite size increases with the temperature, reaching a maximum of 225 ±8 nm for a flash annealing at 170°C for 5 minutes. This particle

growth is well visible on top-view SEM images showing larger grains, reaching a maximum of 486 nm in average for the aforementioned conditions (**Figure 3.b**). This observation is consistent with previous literature indicating that a high temperature annealing affords larger grains size [40].

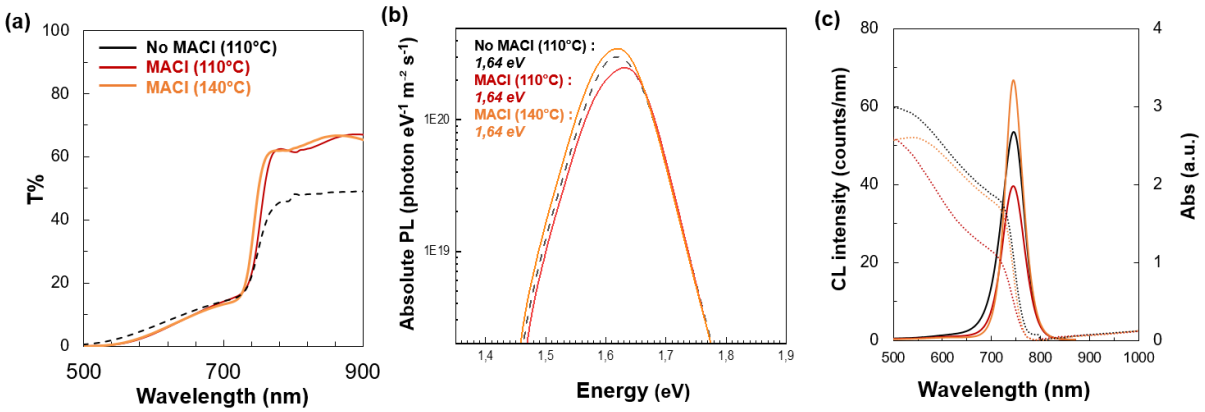

Figure 4: Comparison between MACl-free layer, MACl post-treated at 110°C or 130°C for 30 minutes: (a) Transmission spectra, **(b)** Photoluminescence measurements and **(c)** Cathodo-luminescence spectra (solid curves) associated with the absorption ones (dotted curve).

The optical properties of the perovskite thin films were then investigated for three deposition conditions: a reference sample without MACl additive and annealed at 110°C, and two samples with a MACl: FAI ratio of (0.3:1), annealed at 110°C and 140°C. The general improvement of the perovskite film morphology with MACl addition leads to the increase the sub-bandgap optical transmission, regardless of the annealing temperature (**Figure 4.a**.). From the transmission curves, no noticeable variation of the optical bandgap value can be observed. This is confirmed by the constant bandgap value of 1.64 eV obtained from the fitting of the PL curves, using the model proposed by Katahara et al.[41,42] **(Figure 4.b.)**. High-resolution cathodoluminescence (CL) mappings, that allow to acquire an emission spectrum on every location of the sample surface with a spatial resolution below 100 nm, were performed on the three samples. The averaged CL spectra, integrated over the studied surface are depicted in **Figure 4.c** and the associated integrated CL maps and corresponding SEM images are available in the supplementary materials **(Figure S 2).** For each sample studied, a single characteristic

band at ~750 nm was measured, corresponding to the perovskite emission and being consistent with the related absorbance curve (dotted lines). These results support further that the bandgap remains unchanged, thus excluding once again the possibility of a chloride inclusion that would give rise to a bandgap widening[38]. Moreover, we notice that the addition of MACl associated with an annealing temperature of 140°C lowers the FWHM CL emission band from 57 nm to 46 nm pointing out the enhancement of the perovskite material purity and optical properties [43,44]. Notably, Diab et al. related this emission peak evolution to the reduction of defects incorporation, strain and composition fluctuation [45].

2.3. Devices performances and stability

In order to assess the impact of MACl addition and annealing temperature on the solar cell performances, we fabricated full devices having a n-i-p architecture as follows: glass/FTO/c-TiO_2/m-TiO_2/$Cs_{0.17}FA_{0.83}Pb(I_{0.83}Br_{0.17})_3$/Spiro-OMeTAD/Au. The deposition parameters described in the experimental section, lead to a perovskite layer thickness of 400 - 450 nm, as confirmed by the cross-section SEM images (**Figure 2**). The details of the PV characteristics (best cell and average values performances) for each growth conditions (MACl concentration and annealing conditions) are shown in

Table S 1. We first compared perovskite absorbers layer annealed at 110°C and deposited with or without additive. MACl addition in the ink formulation affords a remarkable increase of the cell average open-circuit voltage (V_{oc}) from 0.99 V to 1.12 V, and of the average short-circuit current density (J_{sc}) from 12.8 mA/cm² to 18.8 mA/cm². Such an important improvement of the PV performances stems mainly from an enhancement of the film quality in terms of morphology, pinholes disappearance, lower level of grain boundaries and smoother surface (**Figure 2**). The highest power conversion efficiency, obtained with a film prepared with MACl: FAI (0.3:1)

molar ratio and a post-annealing temperature of only 110°C for 30 minutes, is 16.8% (V_{oc} = 1.15 V, J_{sc} = 19.8 mA/cm², FF = 74.1 %).

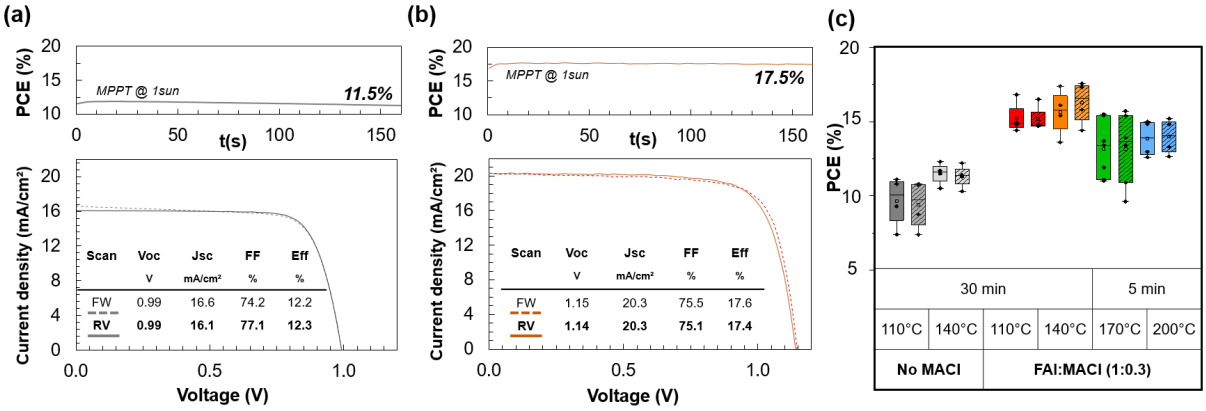

Figure 5 : (J-V) curve and stabilized power output for: (a) Device without MACl addition with a post-annealing treatment at 140°C for 30 minutes, **(b)** Device with MACl: FAI (0.3:1) molar ratio with a post-annealing treatment at 140°C for 30 minutes and **(c)** Device statistics for each crystallization conditions, reverse scan (plain color) and forward scan (stripped).

This power conversion efficiency can be further enhanced increasing the post-annealing temperature up to 140°C. In this case, the stabilized PCE reaches as high as 17.5 % for the champion cell thanks to an improvement of J_{sc} from 18.8 to 19.7 mA/cm² in average without any drop after maximum power point (MPP) tracking under one sun (AM 1.5G) illumination for 150 s (V_{oc} = 1.14V, J_{sc} = 20.3 mA/cm², FF = 75% for reverse scan) (**Figure 5.b.**). Importantly, the devices do not exhibit any hysteretic behavior indicating the high quality of the perovskite layer and the interfaces with both the electron and hole transport layers. Moreover, we have investigated the effect of a flash annealing at high temperature, namely 170 °C and 200 °C. Despite a significant increase of the grains size outlined in the previous part, the flash annealing process did not yield better efficiency than the standard one (**Figure 5.c.**), reaching a maximum efficiency of 15.7% for a post-treatment at 170°C during 5 minutes. Nonetheless, flash annealing is an interesting pathway for industrial fabrication and will be further studied in future works. MPP tracking curves of all fabrication conditions are available in **Figure S** 3. Finally, we have investigated the stability of the devices over 180 hours under

continuous illumination. For each crystallization conditions, encapsulated devices have been fabricated and the evolution of the maximum power point has been tracked, as shown in **Figure 6**. The initial performances have been measured in standard A.M.1.5G conditions, before and just after the encapsulation process to check that the encapsulation process does not impact the cell efficiency.

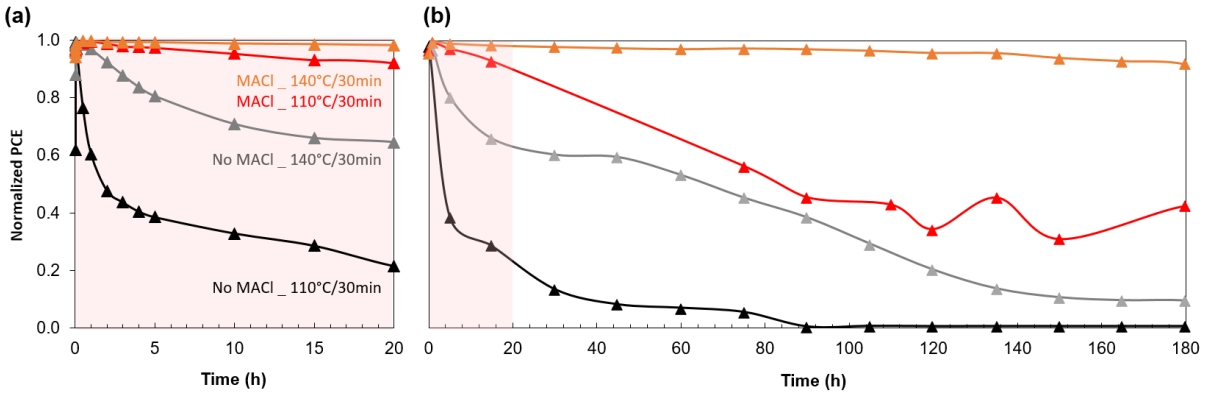

Figure 6 : Normalized PCE under MPP tracking condition of encapsulated devices under continuous illumination: (a) for the first 20 hours of ageing tests and **(b)** Maximum power point tracking curves during180 hours.

Interestingly, in addition to improve the device performances, our results highlight that the MACl has also an important impact on the device stability. Regardless of the annealing temperature, ie. 110°C (black curve) and 140°C (grey curve), the devices fabricated without MACl lost more than 40% of their initial efficiency within the first 20 hours. Conversely, when MACl is introduced into the perovskite precursor ink, the devices exhibit a superior stability which is particularly blatant for a film post-annealed at 140°C (orange curve) which retained more than 90 % of the initial PCE after 180 hours ageing. We realized a post-mortem analysis of the devices and their cross section have been analysed with STEM technique in order to identify the main degradation paths. The images of the lamellae of each sample at lower magnification are displayed in **Figure S** 4. High Annular Angle Dark-Field (HAADF) images show a clear damage of the cell stacks prepared without MACl (**Figure 7.a.**).

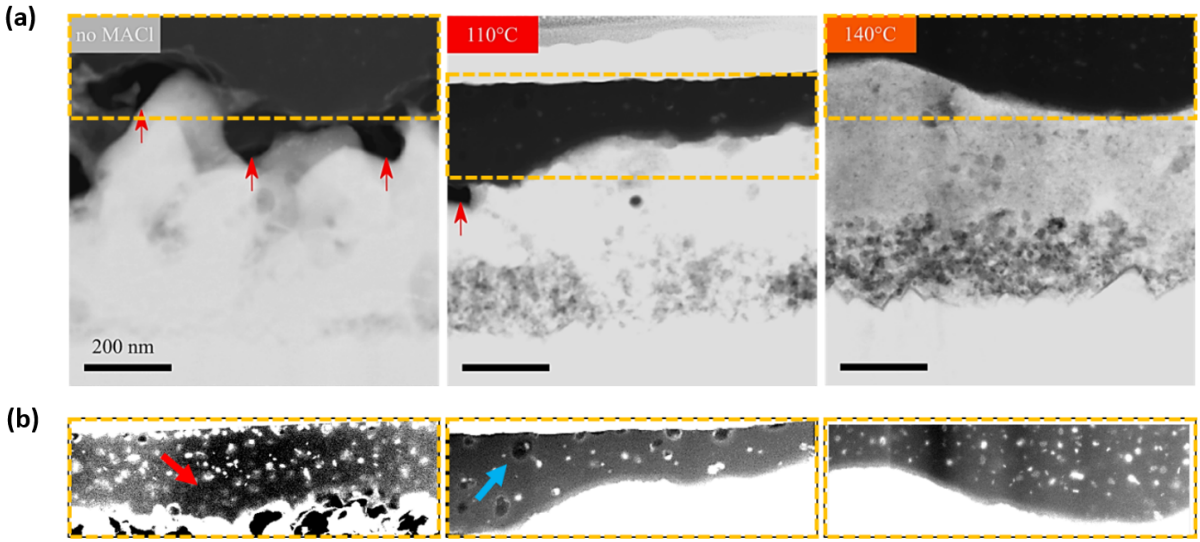

Figure 7: (a) STEM-HAADF images of three different devices: without MACl, with MACl annealed at 110°C and 140°C. Delamination of the Spiro-OMeTAD layer is highlighted by the red arrows. **(b)** Focus on Spiro-OMeTAD (yellow zone) with adjusted contrast.

After ageing under illumination, voids (indicated with red arrows in **Figure 7**) appears at the interface between the perovskite and the Spiro-OMeTAD layers. This delamination seems to be linked to the initial roughness of the film, and is avoided when the annealing temperature is increased (140°C) and MACl used as additives. Indeed, as shown before, these deposition conditions allows for the growth of compacter and smoother films. Besides, by adjusting the contrast on HAADF images (**Figure 7.b.**), the presence of pinholes is detected in Spiro-OMeTAD layer after ageing, for all conditions tested. Interestingly, such degradation of the Spiro-OMeTAD layer have been described by Kim et al [46]. These authors showed that the drop of the cell performances over time can be induced by iodide ions diffusing from the perovskite layer into the spiro-OMeTAD, which changed the electrical properties of the HTL through reduction and decreased charge-carrier collection through the formation of energy barriers. Therefore, the replacement of the spiro-OMeTAD for a PTAA layer could address this issue and enhance the stability of the device in future work. The elemental distribution within the perovskite layer of a champion devices, i.e. with MACl and a post-annealing at 140°C, before

and after ageing has been carried out by Energy Dispersive X-ray Spectroscopy (EDS) in STEM mode.

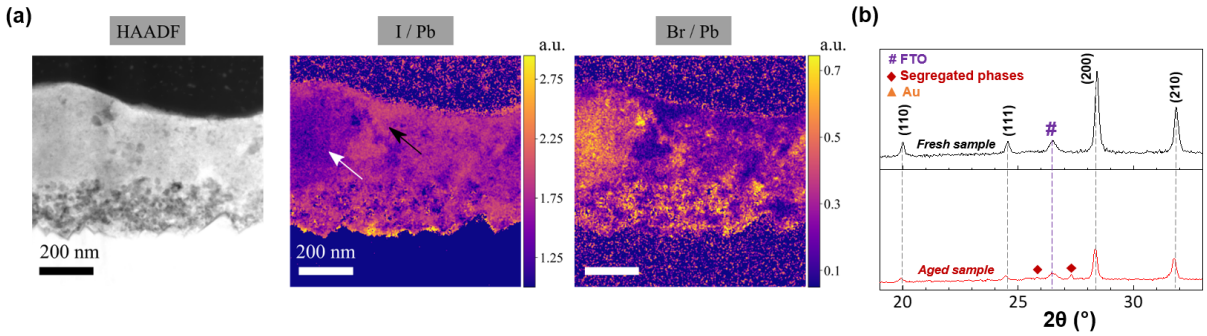

Figure 8: Characterization of the perovskite layer, annealed at 140°C with MACl in precursor ink, in full device configuration. (a) STEM-HAADF images of the device after stability test. STEM-EDS distribution map of the same region. Ratio Iodide/Lead and Bromide/Lead distribution maps are represented. Black and white arrows indicate respectively I-rich and Br-rich region. **(b)** X-ray diffractograms of fresh and aged perovskite layer.

If the fresh sample exhibits a homogeneous elemental distribution with a halide to lead ratio that remains constant along the layer thickness (**Figure S5)**, the aged one, presents both I-rich and Br-rich regions that are pointed out by arrows in the **Figure 8.a**. This phenomenon has been ascribed to a photo-induced phase segregation originating from the thermodynamic metastability of multianions perovskite [47–53], also visible on X-ray diffractograms (**Figure 8.b.**) with the apparition of new peaks at $2\theta = 25.8°$ and $2\theta = 27.3°$. Moreover, as demonstrated by Draguta et al. [50], this phase segregation comes together with a strain relaxation. The wide bandgap regions (i.e. bromide rich regions) may create a significant band bending in contact with the low band gap one (i.e. iodide rich regions) affecting V_{OC} and charge transport [54] inducing a significant drop of the device efficiency.

3. Conclusion

In this study, we proposed a method to fabricate a state-of-the-art double cation high bandgap (1.64eV) perovskite films, utilizing a one-step slot-die-coating process. This process is completed by an addition of MACl and a vacuum aspiration protocol, which is suitable for large

area fabrication of perovskite layers. We compared vacuum extraction and anti-solvent dripping and highlighted the phenomena involved in the perovskite layer formation. We demonstrated that the quench method has a significant impact on the final layer morphology, and thus that the ink composition must be tailored consequently. We explored different MACl concentration and annealing temperatures yielding to an optimization of the device performances reaching a stabilized 17.5 % PCE. These values are among the best reported for slot-die coated high bandgap perovskite. Furthermore, we studied the stability of our devices under constant illumination, demonstrating a good stability after 180h of continuous illumination. After ageing, we observed that the degradation is mainly due to a delamination of the spiro layer and a photo-induced phase segregation, confirmed by the STEM-EDS distribution maps and visible on X-ray diffractograms. This work provides important insights into the link between the perovskite morphology improved by MACl addition and the stability of the devices. These results paves the way to future developments toward modules fabrication and improvements of our encapsulation process.

4. Experimental methods

4.1. Materials

FTO substrates (standard size: 300*300*3 mm) were purchased from Solems. Formamidinium iodide (FAI, ≥ 99% anhydrous), Methylammonium chloride (MACl, ≥ 99%), Lead bromide ($PbBr_2$, 99.99%), Cesium iodide (CsI, 99.99%),), N,N-dimethylformamide (DMF, anhydrous 99.8%) and N-methyl-2-pyrrolidinone (NMP, anhydrous 99.5%), Bis(trifluoromethane)sulfonimide lithium salt (Li-TFSI, 99.95%), 4-tert-butylpyridine (t-BP, 96%) and FK 209 Co(III) TFSI Salt were all purchased from Sigma-Aldrich. PbI_2 was purchased from TCI. The titanium(diisopropoxide) bis(2,4-pentanedionate), 75% in isopropanol was purchased from Alfa Aesar and the titanium dioxide paste 30NR-D from GreatCellsolar. 2,2',7,7'-tetrakis [N,N-di (4-methoxyphenyl)amino]-9,9'-spirobifluorene (Spiro-OMeTAD) were purchased from Borun New Materials. All materials were used as received without further purification.

4.2. Solar cells fabrication

The FTO substrates are successively washed with soap during 45 minutes at 60°C, acetone, and ethanol, for 20 minutes each in ultrasound bath. Then, they are treated under UV-ozone for 15 minutes before an annealing at 500°C for 30 minutes. The electron transport layer (c-TiO_2) is made using titanium(diisopropoxide) mixed with acetyl acetone and IPA, and deposited by spray pyrolysis on FTO substrates on a hotplate at 450°C. The mesoporous TiO_2 is spin-coated on the compact at 4000 rpm for 30s, then annealed at 125°C for 5 minutes, 325°C for 15 minutes, 375°C for 5 minutes, 450°C for 5 minutes and 500°C for 5 minutes. The perovskite ink precursor solutions are prepared in a glovebox, with various MACl concentrations. Typically, the ink recipe is formulated by 1.49 g of $PbBr_2$, 5.47 mg of PbI_2, 2.27 mg of FAI, and 0.70 g of CsI in a solution of NMP: DMF (1: 10, v/v), plus the amount of MACl corresponding at

MACl: FAI (0.15:1 or 0.3:1)mol. The perovskite precursor solution is stirred at 60°C overnight. For slot-die deposition, the as-prepared perovskite ink is filtered by 0.4 µm PTFE filter and directly filled into the ink bottle tank of nTact slot-die at room temperature in glovebox. The coating parameters are developed ahead of the study and kept identical for all the coatings: the coating speed range is 5-15 mm/s, the coating gap is 30-60 µm and injection rate is 2-4 µL/s. Right after the coating, the deposited substrates are immediately transferred into a vacuum chamber for pumping down to 0.7 mbar during 5 minutes. Afterwards, the quenched substrates are annealed on a hotplate. After cooling down to room temperature, Spiro-OMeTAD acting as hole transport material is spin-coated onto the perovskite surface at 3000 rpm for 35s. Spiro-OMeTAD solution is prepared by dissolving 110 mg Spiro-OMeTAD in 1mL of chlorobenzene. Then, we add 45 µL of commercial solution 4-tert-Butylpyridine (TBP), 25 µL of lithium bis(trifluoromethanesulfonyl)imide (LiTFSI) stock solution (520 mg/mL LiTFSI in acetonitrile (ACN)) and 17 µL of a Cobalt stock solution (400 mg of FK209 in 1mL of ACN). Finally, 100 nm of gold is evaporated on top of the Spiro-OMeTAD layer by e-beam evaporator.

4.3. Encapsulation

The devices are first encapsulated with a surlyn polymer and a 1mm sodosilicate glass. This stack is put into a vacuum press and heated at 100°C during 2 minutes. Then, we add a Loctite glue as an edge sealant. This glue is cured under UV during 1 minute exposition. During this exposition, the perovskite part is protected by a dark mask. The cell contacts are extended outside the encapsulation by copper tape.

4.4. Characterization

Scanning electron microscopy images are performed using a Zeiss Merlin to visualize the morphology of the perovskite films. The Panalytical X-ray diffraction (XRD) analyzer is used to characterize the crystal structure of perovskite thin film (Cu $K\alpha_1\alpha_2$ radiation, λ=1.5418 Å).

A filtered Xenon lamp simulator 3A (Newport, 300 W) was used to characterize the current density-voltage (J-V) curve with the light intensity in 100 $mW.cm^{-2}$ under a AM 1.5 G solar spectrum filter condition in the ambient. The J-V curves were obtained under both reverse and forward scanning in the span from 1.2 to -0.2 V at ~ 20 mV/s with a computer-controlled Keithley. The device area was defined by a metal mask of 0.09cm^2. Devices were typically exposure to light source for ~ 30 sec for light soaking before scanning. The microscope images was acquired with a confocal microscope Olympus LEXT OLS5100 and the Sa value was extracted by 3D acquisition of the sample surface (129x129μm^2 area). UV-visible absorption, transmission and reflexion spectra were measured with a Cary 5000 ultraviolet-visible (UV/Vis) spectrometer. PL spectra were acquired with a hyperspectral imaging system that records luminescence intensity signal along three dimensions $\{x,y,\lambda\}$. Its mains components are: a home built microscope with Thorlabs optomechanical elements, a 2D bandpass filtering system from company PhotonEtc with 2nm resolution and finally a 1Mpix silicon-based CCD camera PCO1300. The sample is illuminated (λ=532nm) through 50x Nikon objective and the luminescence is collected through the same objective. The excitation beam and luminescence signals are separated with appropriate dichroic beam splitter and filters. Cathodoluminescence measurements are performed using an Attolight Chronos quantitative cathodoluminescence microscope at room temperature with 3kV acceleration voltage and a dose lower than 10^{20} e^-/cm^2. Lamellae preparation was done with a FEI Dual-Beam Helios. We used the FEI standard procedure for the specimen thinning (which avoid most of ion-induced degradation). To investigate these specimens, a FEI Osiris TEM was used in STEM mode. Acceleration voltage was kept at 200kV and current < 500 pA during EDS and HAADF acquisition.

Acknowledgements

This project has been supported by the French Government in the frame of the program of investment for the future (Programme d'Investissement d'Avenir - ANR-IEED-002-01). S.C. would like to thank funding from the European Union's Horizon 2020 research and innovation programme under the Marie Skłodowoska-Curie Grant Agreement N 845612.

5. References

[1] A. Kojima, K. Teshima, Y. Shirai, T. Miyasaka, *J. Am. Chem. Soc.* **2009**, *131*, 6050.
[2] J. Jeong, M. Kim, J. Seo, H. Lu, P. Ahlawat, A. Mishra, Y. Yang, M. A. Hope, F. T. Eickemeyer, M. Kim, Y. J. Yoon, I. W. Choi, B. P. Darwich, S. J. Choi, Y. Jo, J. H. Lee, B. Walker, S. M. Zakeeruddin, L. Emsley, U. Rothlisberger, A. Hagfeldt, D. S. Kim, M. Grätzel, J. Y. Kim, *Nature* **2021**, DOI 10.1038/s41586-021-03406-5.
[3] Y. Galagan, *The Journal of Physical Chemistry Letters* **2018**, *9*, 4326.
[4] Y. Deng, E. Peng, Y. Shao, Z. Xiao, Q. Dong, J. Huang, *Energy & Environmental Science* **2015**, *8*, 1544.
[5] R. Munir, **n.d.**, 221.
[6] J. Yin, Y. Lin, C. Zhang, J. Li, N. Zheng, *ACS Applied Materials & Interfaces* **2018**, *10*, 23103.
[7] Y. Zhong, R. Munir, J. Li, M.-C. Tang, M. R. Niazi, D.-M. Smilgies, K. Zhao, A. Amassian, *ACS Energy Letters* **2018**, *3*, 1078.
[8] Y. Deng, C. H. Van Brackle, X. Dai, J. Zhao, B. Chen, J. Huang, *Sci. Adv.* **2019**, *5*, eaax7537.
[9] F. Mathies, H. Eggers, B. S. Richards, G. Hernandez-Sosa, U. Lemmer, U. W. Paetzold, *ACS Applied Energy Materials* **2018**, *1*, 1834.
[10] Z. Li, P. Li, G. Chen, Y. Cheng, X. Pi, X. Yu, D. Yang, L. Han, Y. Zhang, Y. Song, *ACS Appl. Mater. Interfaces* **2020**, acsami.0c09485.
[11] Z. Bi, Z. Liang, X. Xu, Z. Chai, H. Jin, D. Xu, J. Li, M. Li, G. Xu, *Solar Energy Materials and Solar Cells* **2017**, *162*, 13.
[12] Y. Jiang, C. Wu, L. Li, K. Wang, Z. Tao, F. Gao, W. Cheng, J. Cheng, X.-Y. Zhao, S. Priya, W. Deng, *Nano Energy* **2018**, *53*, 440.
[13] C. Zuo, D. Vak, D. Angmo, L. Ding, M. Gao, *Nano Energy* **2018**, *46*, 185.
[14] M. Remeika, L. K. Ono, M. Maeda, Z. Hu, Y. Qi, *Organic Electronics* **2018**, *54*, 72.
[15] J.-E. Kim, Y.-S. Jung, Y.-J. Heo, K. Hwang, T. Qin, D.-Y. Kim, D. Vak, *Solar Energy Materials and Solar Cells* **2018**, *179*, 80.
[16] F. Di Giacomo, S. Shanmugam, H. Fledderus, B. J. Bruijnaers, W. J. H. Verhees, M. S. Dorenkamper, S. C. Veenstra, W. Qiu, R. Gehlhaar, T. Merckx, T. Aernouts, R. Andriessen, Y. Galagan, *Solar Energy Materials and Solar Cells* **2018**, *181*, 53.
[17] J. B. Whitaker, D. H. Kim, B. W. Larson, F. Zhang, J. J. Berry, M. F. A. M. van Hest, K. Zhu, *Sustainable Energy Fuels* **2018**, *2*, 2442.
[18] Y.-J. Heo, J.-E. Kim, H. Weerasinghe, D. Angmo, T. Qin, K. Sears, K. Hwang, Y.-S. Jung, J. Subbiah, D. J. Jones, M. Gao, D.-Y. Kim, D. Vak, *Nano Energy* **2017**, *41*, 443.
[19] T. Qin, W. Huang, J.-E. Kim, D. Vak, C. Forsyth, C. R. McNeill, Y.-B. Cheng, *Nano Energy* **2017**, *31*, 210.
[20] F. Xu, J. Liu, A. S. Subbiah, W. Liu, J. Kang, G. T. Harrison, X. Yang, F. H. Isikgor, E. Aydin, M. De Bastiani, S. De Wolf, *Small Science* **2021**, 2000044.
[21] X. Ding, J. Liu, T. A. L. Harris, *AIChE Journal* **2016**, *62*, 2508.
[22] D. Burkitt, J. Searle, D. Worsley, T. Watson, *Materials* **2018**, *11*, 2106.
[23] C. Liu, Y.-B. Cheng, Z. Ge, *Chem. Soc. Rev.* **2020**, *49*, 1653.
[24] X. Li, D. Bi, C. Yi, J.-D. Decoppet, J. Luo, S. M. Zakeeruddin, A. Hagfeldt, M. Gratzel, *Science* **2016**, *353*, 58.
[25] B. Ding, L. Gao, L. Liang, Q. Chu, X. Song, Y. Li, G. Yang, B. Fan, M. Wang, C. Li, C. Li, *ACS Applied Materials & Interfaces* **2016**, *8*, 20067.
[26] M. Yang, Z. Li, M. O. Reese, O. G. Reid, D. H. Kim, S. Siol, T. R. Klein, Y. Yan, J. J. Berry, M. F. A. M. van Hest, K. Zhu, *Nature Energy* **2017**, *2*, 17038.

[27] M. Mateen, Z. Arain, Y. Yang, X. Liu, S. Ma, C. Liu, Y. Ding, X. Ding, M. Cai, S. Dai, *ACS Appl. Mater. Interfaces* **2020**, *12*, 10535.
[28] M. Kim, G.-H. Kim, T. K. Lee, I. W. Choi, H. W. Choi, Y. Jo, Y. J. Yoon, J. W. Kim, J. Lee, D. Huh, H. Lee, S. K. Kwak, J. Y. Kim, D. S. Kim, *Joule* **2019**, *3*, 2179.
[29] F. Guo, S. Qiu, J. Hu, H. Wang, B. Cai, J. Li, X. Yuan, X. Liu, K. Forberich, C. J. Brabec, Y. Mai, *Adv. Sci.* **2019**, *6*, 1901067.
[30] B. Li, M. Li, C. Fei, G. Cao, J. Tian, *Journal of Materials Chemistry A* **2017**, *5*, 24168.
[31] M. Wang, B. Li, P. Siffalovic, L.-C. Chen, G. Cao, J. Tian, *J. Mater. Chem. A* **2018**, *6*, 15386.
[32] K. Odysseas Kosmatos, L. Theofylaktos, E. Giannakaki, D. Deligiannis, M. Konstantakou, T. Stergiopoulos, *Energy Environ. Mater.* **2019**, *2*, 79.
[33] C. Li, Y. Zhou, L. Wang, Y. Chang, Y. Zong, L. Etgar, G. Cui, N. P. Padture, S. Pang, *Angew. Chem. Int. Ed.* **2017**, *56*, 7674.
[34] Z. Arain, C. Liu, Y. Yang, M. Mateen, Y. Ren, Y. Ding, X. Liu, Z. Ali, M. Kumar, S. Dai, *Sci. China Mater.* **2019**, *62*, 161.
[35] F. Cheng, X. Jing, R. Chen, J. Cao, J. Yan, Y. Wu, X. Huang, B. Wu, N. Zheng, *Inorg. Chem. Front.* **2019**, *6*, 2458.
[36] Y.-H. Seo, E.-C. Kim, S.-P. Cho, S.-S. Kim, S.-I. Na, *Applied Materials Today* **2017**, *9*, 598.
[37] Y. Li, T. Zhang, F. Xu, Y. Wang, G. Li, Y. Yang, Y. Zhao, *Crystals* **2017**, *7*, 272.
[38] J. Xu, C. C. Boyd, Z. J. Yu, A. F. Palmstrom, D. J. Witter, B. W. Larson, R. M. France, J. Werner, S. P. Harvey, E. J. Wolf, W. Weigand, S. Manzoor, M. F. A. M. van Hest, J. J. Berry, J. M. Luther, Z. C. Holman, M. D. McGehee, *Science* **2020**, *367*, 1097.
[39] F. Xie, *Environmental Science* **2017**, 8.
[40] M. Kim, G.-H. Kim, K. S. Oh, Y. Jo, H. Yoon, K.-H. Kim, H. Lee, J. Y. Kim, D. S. Kim, *ACS Nano* **2017**, *11*, 6057.
[41] S. Cacovich, D. Messou, A. Bercegol, S. Béchu, A. Yaiche, H. Shafique, J. Rousset, P. Schulz, M. Bouttemy, L. Lombez, *ACS Appl. Mater. Interfaces* **2020**, *12*, 34784.
[42] J. K. Katahara, H. W. Hillhouse, *J. Appl. Phys.* **2014**, *116*, 173504.
[43] C. Xiao, Z. Li, H. Guthrey, J. Moseley, Y. Yang, S. Wozny, H. Moutinho, B. To, J. J. Berry, B. Gorman, Y. Yan, K. Zhu, M. Al-Jassim, *J. Phys. Chem. C* **2015**, 8.
[44] T. Paul, B. K. Chatterjee, S. Maiti, S. Sarkar, N. Besra, B. K. Das, K. J. Panigrahi, S. Thakur, U. K. Ghorai, K. K. Chattopadhyay, *J. Mater. Chem. C* **2018**, *6*, 3322.
[45] H. Diab, C. Arnold, F. Lédée, G. Trippé-Allard, G. Delport, C. Vilar, F. Bretenaker, J. Barjon, J.-S. Lauret, E. Deleporte, D. Garrot, *J. Phys. Chem. Lett.* **2017**, *8*, 2977.
[46] S. Kim, S. Bae, S.-W. Lee, K. Cho, K. D. Lee, H. Kim, S. Park, G. Kwon, S.-W. Ahn, H.-M. Lee, Y. Kang, H.-S. Lee, D. Kim, *Sci Rep* **2017**, *7*, 1200.
[47] E. T. Hoke, D. J. Slotcavage, E. R. Dohner, A. R. Bowring, H. I. Karunadasa, M. D. McGehee, *Chem. Sci.* **2015**, *6*, 613.
[48] C. G. Bischak, C. L. Hetherington, H. Wu, S. Aloni, D. F. Ogletree, D. T. Limmer, N. S. Ginsberg, *Nano Lett.* **2017**, *17*, 1028.
[49] S. J. Yoon, S. Draguta, J. S. Manser, O. Sharia, W. F. Schneider, M. Kuno, P. V. Kamat, *ACS Energy Lett.* **2016**, *1*, 290.
[50] S. Draguta, O. Sharia, S. J. Yoon, M. C. Brennan, Y. V. Morozov, J. S. Manser, P. V. Kamat, W. F. Schneider, M. Kuno, *Nat Commun* **2017**, *8*, 200.
[51] K. A. Bush, K. Frohna, R. Prasanna, R. E. Beal, T. Leijtens, S. A. Swifter, M. D. McGehee, *ACS Energy Lett.* **2018**, *3*, 428.
[52] V. Kumar, W. L. Schmidt, G. Schileo, R. C. Masters, M. Wong-Stringer, D. C. Sinclair, I. M. Reaney, D. Lidzey, C. Rodenburg, *ACS Omega* **2017**, *2*, 2126.

[53] T. Duong, H. K. Mulmudi, Y. Wu, X. Fu, H. Shen, J. Peng, N. Wu, H. T. Nguyen, D. Macdonald, M. Lockrey, T. P. White, K. Weber, K. Catchpole, *ACS Appl. Mater. Interfaces* **2017**, *9*, 26859.
[54] O. Hentz, Z. Zhao, S. Gradečak, *Nano Lett.* **2016**, *16*, 1485.

Sophie Bernard*, Salim Mejaouri*, Stefania Cacovich, Sébastien Jutteau, Iwan Zimmerman, Armelle Yaiche, Stéphanie Gbegnon, Dominique Loisnard, Stéphane Collin, Aurélien Duchatelet, Frederic Sauvage, Jean Rousset

One-step slot-die coating deposition of wide-bandgap perovskite absorber for efficient solar cells

TOC figure

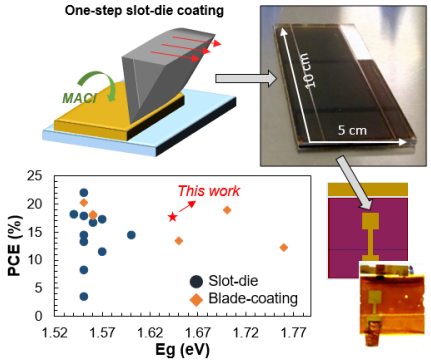

Supporting Information

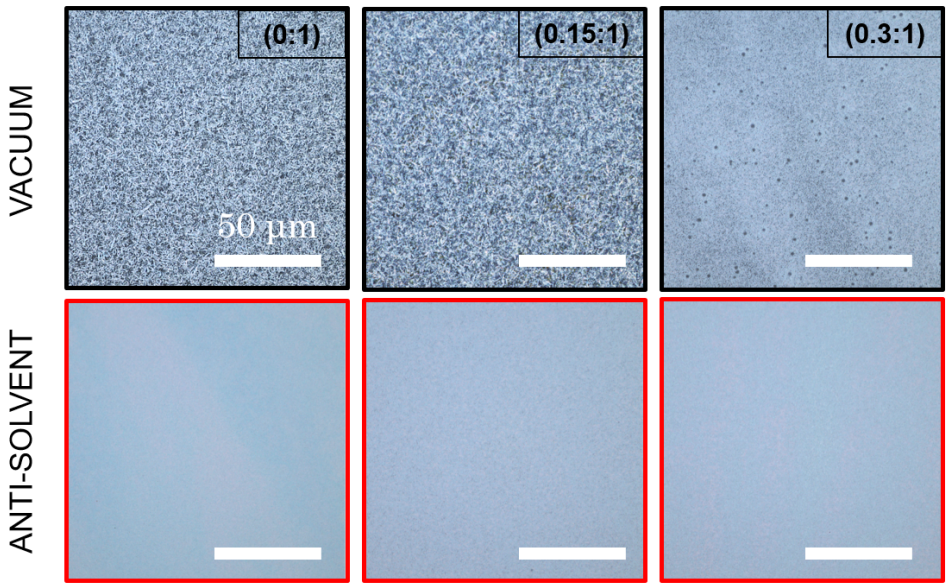

Figure S 1 : Confocal images after annealing at 110°C during 30 min

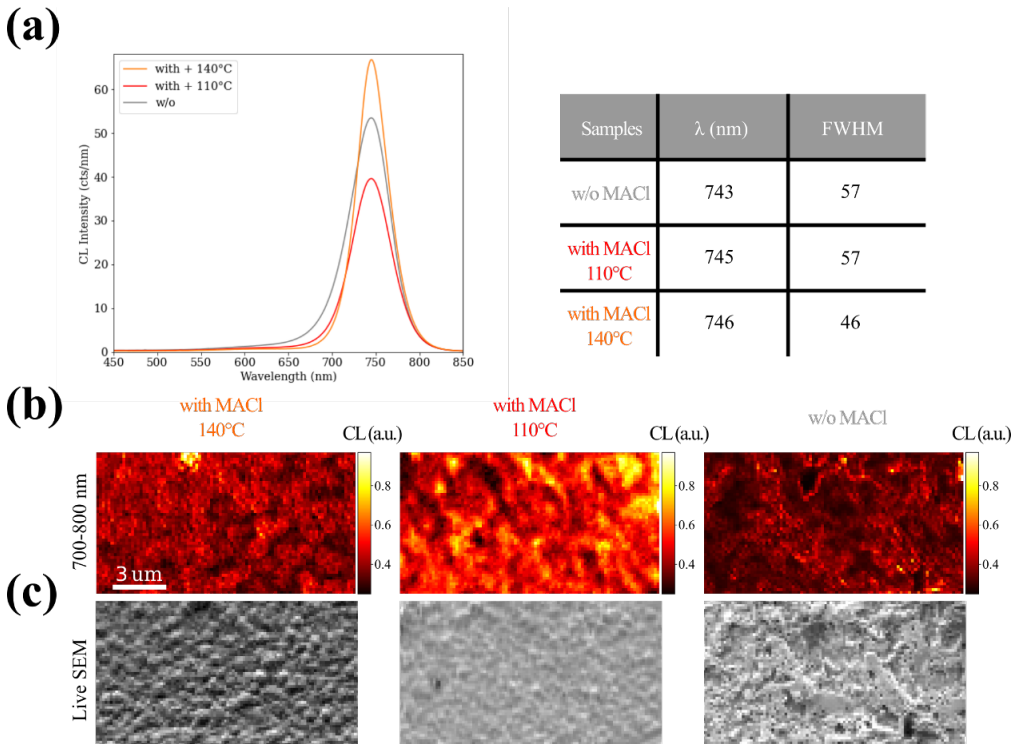

Samples	λ (nm)	FWHM
w/o MACl	743	57
with MACl 110°C	745	57
with MACl 140°C	746	46

Figure S 2 : a. CL spectra of slot-die coated films (Table: wavelength of the CL emission peak, and full width at half maximum FWHM), **b.** Maps of the CL intensity integrated over the Perovskite emission peak (700-850 nm) and **c.** Top-view SEM images of the same areas taken before the CL measurement.

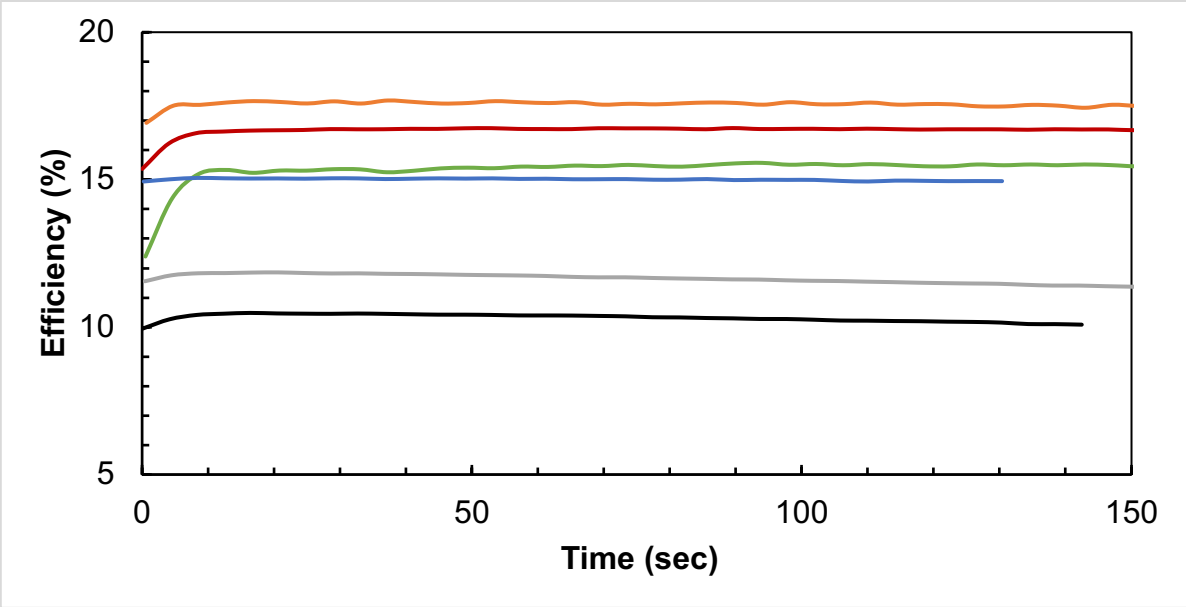

Figure S 3 : MPP tracking of best perovskite devices for each studied conditions

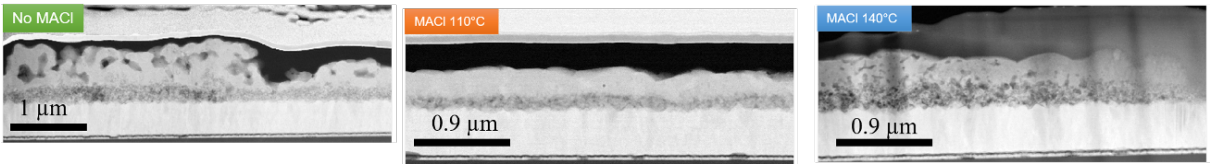

Figure S 4 : STEM-HAADF images of lamellae fabricated from fresh devices: without MACl, with MACl annealed at 110°C and 140°C. The last specimen exhibits "curtaining" – thickness variations - due to FIB preparation.

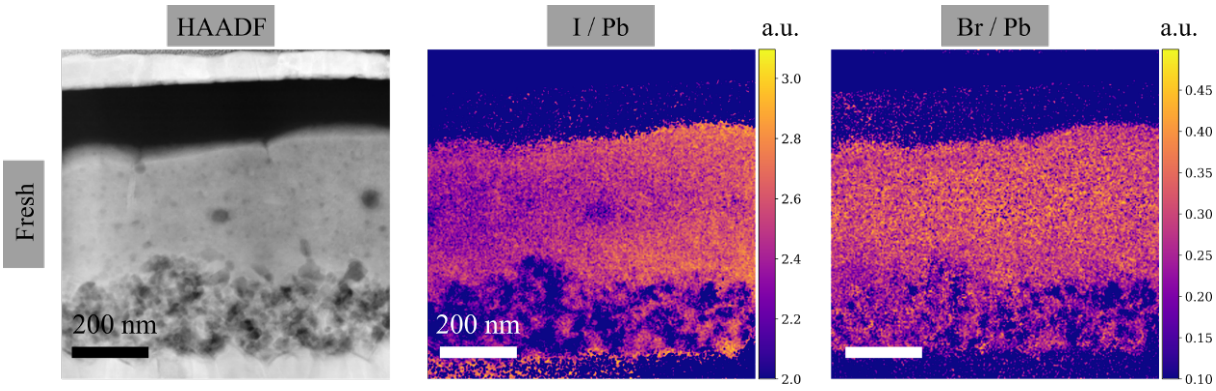

Figure S 5: STEM-HAADF image of lamella fabricated from fresh sevice with MACl annealed at 140°C (best device). Quantitative elemental maps of halide over lead ratio: Iodide / Lead and Bromide / Lead in arbitrary units (% atomic / % atomic)

Table S 1: Full devices performances under different annealing conditions

	Annealing conditions		Voc	Jsc	FF	PCE	Voc	Jsc	FF	PCE
			V	mA/cm²	%	%	V	mA/cm²	%	%
			Reverse				Forward			
No MACl	110°C	Best cell	1.00	14.2	77.5	11.1	1.00	14.6	73.3	10.8
		Average	0.99	12.8	76.7	9.7	0.99	13.0	73.0	9.4
	140°C	Best cell	0.99	16.1	77.2	12.3	0.99	16.6	74.2	12.2
		Average	0.99	15.0	77.7	11.5	0.99	15.5	73.8	11.3
MACl:FAI (0,30:1)	110°C	Best cell	1.15	19.8	74.1	16.8	1.14	19.8	72.9	16.5
		Average	1.12	18.8	72.1	15.2	1.13	18.9	71.1	15.2
	140°C	Best cell	**1.14**	**20.3**	**75.1**	**17.4**	**1.14**	**20.3**	**75.5**	**17.6**
		Average	1.10	19.7	72.4	15.6	1.11	19.7	74.3	16.3
	170°C	Best cell	1.09	19.4	72.7	15.4	1.10	19.6	73.0	15.7
		Average	1.09	16.3	70.0	13.5	1.07	18.1	64.6	12.7
	200°C	Best cell	1.07	19.1	74.1	15.0	1.70	19.1	74.6	15.2
		Average	1.09	17.6	72.3	13.9	1.25	17.6	72.5	14.0